

DEEP LOW-RANK PLUS SPARSE NETWORK FOR DYNAMIC MR IMAGING

A PREPRINT

Wenqi Huang^{1,3}, Ziwen Ke^{1,3}, Zhuoxu Cui¹, Jing Cheng², Zhilang Qiu^{2,3}, Sen Jia², Yanjie Zhu², and Dong Liang^{1,2*}

¹Research Center for Medical AI, Shenzhen Institutes of Advanced Technology, Chinese Academy of Sciences, Shenzhen, China

²Paul C. Lauterbur Research Center for Biomedical Imaging, Shenzhen Institutes of Advanced Technology, Chinese Academy of Sciences, Shenzhen, China

³Shenzhen College of Advanced Technology, University of Chinese Academy of Sciences, Shenzhen, China

October 27, 2020

ABSTRACT

In dynamic MR imaging, L+S decomposition, or robust PCA equivalently, has achieved stunning performance. However, the selection of parameters of L+S is empirical, and the acceleration rate is limited, which are the common failings of iterative CS-MRI reconstruction methods. Many deep learning approaches were proposed to address these issues, but few of them used the low-rank prior. In this paper, a model-based low-rank plus sparse network, dubbed as L+S-Net, is proposed for dynamic MR reconstruction. In particular, we use an alternating linearized minimization method to solve the optimization problem with low-rank and sparse regularization. A learned soft singular value thresholding is introduced to make sure the clear separation of L component and S component. Then the iterative steps is unrolled into a network whose regularization parameters are learnable. Experiments on retrospective and prospective cardiac cine dataset show that the proposed model outperforms the state-of-the-art CS and existing deep learning methods.

Keywords Compressed sensing · Dynamic MR imaging · Deep learning · Image reconstruction

1 Introduction

Dynamic MR Imaging plays a critical role in clinical application because of its capability to reveal the spatial structure and the dynamic changes in the time dimension simultaneously. The trade-off between spatial resolution and time resolution must be made due to the limited scan time in practice. To resolve the conflict, accelerating dynamic MRI with highly undersampled k-space has raised tremendous research interest.

Over the past decade, the application of compressed sensing (CS) significantly increased the MR imaging speed and efficiency because of its capability to reconstruct images from highly undersampled signals. Sparse prior is widely used in CS-based reconstruction methods. Studies at the early stage used fixed basis such as temporal Fourier transform and Wavelet transforms to sparsify images in the x-t domain [Donoho, 2006, Lustig et al., 2007, Otazo et al., 2010, Ma et al., 2008]. The proposal of dictionary learning and manifold learning pushed the research a step forward. In dictionary learning, the fixed basis was replaced by a learned adaptive basis from acquired data, which led to superior reconstruction performance to the fixed basis methods [Wang and Ying, 2013, Caballero et al., 2014, Nakarmi et al., 2015]. Most recently, major advances in deep-learning-based methods demonstrated great potential in fast MR imaging. Given enough data, deep learning methods will greatly improve the quality of the reconstructed image. These methods can be generally categorized as unrolling-based algorithms [Schlemper et al., 2017, Qin et al., 2018, Wang et al., 2019]

*dong.liang@siat.ac.cn

and those not unrolled [Wang et al., 2016, Kwon et al., 2017, Han et al., 2018, Wang et al., 2020]. Both of these two types have a much more relaxed constraint than the traditional CS methods and the dictionary learning/manifold learning methods. The methods not based on unrolling exploited the specific standard network to learn an end-to-end mapping from undersampled k-space and the clean image, thus usually requires a large number of training data and long training time. In unrolled methods, the iterative CS reconstruction algorithms were unrolled into deep networks to learn the parameters and transforms in the reconstruction model, which means that such networks can perform well with a smaller size of training data [Cheng et al., 2019, Liang et al., 2020]. Furthermore, the end-to-end mapping in the non-unrolled methods are less interpretable than the model-based ones. Therefore the unrolled network are more popular in the MR reconstruction field.

Along with the development of sparse prior, low-rank prior was introduced as an extension of sparsity in two forms: L&S [Lingala et al., 2011, Zhao et al., 2012] and L+S [Candès et al., 2011, Chandrasekaran et al., 2011, Otazo et al., 2015]. Previous works on L&S aimed to find a solution that is both low rank and sparse, while the works on L+S decomposed the data matrix into a low-rank component (L) and a sparse component (S). The L+S decomposition, or Robust Principal Component Analysis (RPCA) equivalently, is more natural for dynamic imaging because the L and the S component can represent the slowly-changing background and the dynamic foreground respectively [Otazo et al., 2015]. The works based on low-rank matrix completion have proved that dynamic MR images have a strong low-rank prior, which can be used to improve the reconstruction quality [Lustig et al., 2010, Gao et al., 2011, Otazo et al., 2015]. Due to the appropriate modeling, L+S has achieved successful applicants in lots of fields besides MR imaging, such as foreground and background separation in computer vision [Candès et al., 2011, Mansour and Vetro, 2014], clutter suppressing in Ultrasound Flow imaging [Ashikuzzaman et al., 2019], and image alignment [Peng et al., 2012]. However, the low-rank prior also brings more parameters to tune in the reconstruction, which exacerbated the empirical selection of the regularization parameters. Besides, the singular value decomposition performed at each iteration is time consuming, which runs against the speed requirement of fast imaging in practice.

In this paper, we aim to eliminate the drawbacks of the L+S method by unrolling it into a deep network. Herein, we proposed a deep low-rank-plus-sparse network (L+S-Net) for dynamic MRI reconstruction. First, we formulated the dynamic MR image as a low-rank plus sparse model under the framework of CS. Then an alternating linearized minimization method was adopted to solve the optimization problem, and the recovery of the L component and the S component can be written into iterative form, in which the low-rank constraint corresponds to a singular value thresholding (SVT). We unrolled the tedious iterative steps into an n -block network and set n as a relatively small integer, leading to a considerable reduction to reconstruction time. All the regularization parameters in the L+S model were set learnable, including the learned singular value thresholding (LSVT), the updating step size and the proximal operator, refraining from the empirical selection. Our method outperforms state-of-the-art deep learning methods on two in vivo cardiac cine datasets, for retrospective and prospective study respectively. We also compared the proposed L+S-Net with traditional L+S to demonstrate the improvement. To the best of our knowledge, this is the first time that deep low-rank prior is applied in multi-coil dynamic MR imaging.

The remaining part of the paper proceeds as follows: Section II provides the background and introduces the proposed methods. Section III summarizes experimental details and the results to demonstrate the effectiveness of the proposed method, while the discussion and conclusions are presented in Section IV and Section V, respectively.

2 Methodology

2.1 Problem formulation

A typical linear imaging model for MRI can be written as

$$\mathbf{A}\mathbf{x} = \mathbf{y} \quad (1)$$

where $\mathbf{A} : \mathbb{C}^N \rightarrow \mathbb{C}^M$ is the encoding matrix, $\mathbf{y} \in \mathbb{C}^M$ is the undersampled k-space data measured during acquisition, \mathbf{x} is the vectorized image to be reconstructed. The encoding matrix \mathbf{A} is decided by the acquisition protocol, which is already known. In single-coil imaging, the encoding matrix $\mathbf{A} = \mathbf{F}_u$, where \mathbf{F}_u is a Fourier transform with undersampling. When it comes to parallel imaging, $\mathbf{A} = \mathbf{F}_u \mathbf{S}$, where \mathbf{S} denotes the coil sensitivities. In such scenarios, the problem of image reconstruction is to recover a clean image \mathbf{x} from the undersampled data \mathbf{y} . According to the Nyquist-Shannon sampling theorem, if the k-space data is so undersampled that it does not satisfy the Nyquist sampling criterion, the reconstruction is hard to accomplish. While the MR image \mathbf{x} has some priors, such as sparse prior, which means it could be sparse under a particular transform \mathbf{D} . CS-base methods can break the sampling theorem by exploiting the sparse representation of the signal. With the help of regularization terms, iterative optimization algorithms are often used to solve the underdetermined inverse problem:

$$\min \|\mathbf{D}\mathbf{x}\|_1, \quad s.t. \quad \mathbf{y} = \mathbf{A}\mathbf{x} \quad (2)$$

The constrained optimization can be reduced to a equivalent unconstrained problem, so the optimal reconstruction image \mathbf{x}^* can be achieved:

$$\mathbf{x}^* = \arg \min_{\mathbf{x}} \frac{1}{2} \|\mathbf{A}\mathbf{x} - \mathbf{y}\|_2^2 + \lambda \|\mathbf{D}\mathbf{x}\|_1 \quad (3)$$

where the second term is a prior regularization with a specific sparsifying transform \mathbf{D} (for example, Wavelet), and λ is the regularization parameter.

2.2 L+S decomposition in dynamic MRI reconstruction

In dynamic MRI, we usually formulate the image as a matrix instead of a vector. Each column of the image matrix represents a vectorized temporal frame. The L+S algorithm decomposes the image matrix \mathbf{X} as a superposition of the background component \mathbf{L} which is assumed to be slowly changing among frames, and the dynamic component \mathbf{S} [Otazo et al., 2015]. Because the background components of each frame have a strong correlation along the temporal dimension, the \mathbf{L} components is a low-rank matrix. The dynamic component \mathbf{S} , which is already sparser than the original image \mathbf{X} with the background suppressed, has a much more sparser representation when the proper sparse transform is performed. In optimization, nuclear norm, which is the sum of the singular values of the matrix, has been used as a good surrogate for minimizing the rank. Therefore, the optimization problem in Eq.(3) can be written in the L+S form:

$$\min_{\mathbf{L}, \mathbf{S}} \frac{1}{2} \|\mathbf{A}(\mathbf{L} + \mathbf{S}) - \mathbf{y}\|_2^2 + \lambda_L \|\mathbf{L}\|_* + \lambda_S \|\mathbf{D}\mathbf{S}\|_1 \quad (4)$$

where \mathbf{D} represents the sparse transform, and λ_L and λ_S are the regularization parameters of low-rank term and sparse term respectively. They together control the proportion between the background componet \mathbf{L} and the dynamic componet \mathbf{S} .

2.3 The proposed method: L+S Network for dymanic imaging

In order to solve the optimization problem in Eq.(4), we introducing a auxiliary variable \mathbf{X} , which denotes the image to be reconstructed or the superposition of the \mathbf{L} component and the \mathbf{S} component equivalently. The reformed optimization problem is as follow

$$\min_{\mathbf{L}, \mathbf{S}, \mathbf{X}} \frac{1}{2} \|\mathbf{A}\mathbf{X} - \mathbf{y}\|_2^2 + \lambda_L \|\mathbf{L}\|_* + \lambda_S \|\mathbf{D}\mathbf{S}\|_1, \quad s.t. \quad \mathbf{X} = \mathbf{L} + \mathbf{S}. \quad (5)$$

The auxiliary is specially described for the our proposed L+S-Net. The introduction of the auxiliary variable \mathbf{X} enables a inexact search of \mathbf{L} and \mathbf{S} at the beginning of the iteration steps, which makes it faster to find optimal \mathbf{L} and \mathbf{S} . This is critical in unrolled deep learning methods. The number of iteration blocks in unrolled network is much fewer than the iteration steps needed to converge in iterative methods; When unrolled into the network, the inital steps of the search will play a important role in finding optimal points. The penalty function of Eq.(5) is:

$$J(\mathbf{X}, \mathbf{L}, \mathbf{S}) = \frac{1}{2} \|\mathbf{A}\mathbf{X} - \mathbf{y}\|_2^2 + \lambda_L \|\mathbf{L}\|_* + \lambda_S \|\mathbf{D}\mathbf{S}\|_1 + \frac{\rho}{2} \|\mathbf{L} + \mathbf{S} - \mathbf{X}\|_2^2 \quad (6)$$

where $\frac{\rho}{2}$ is a penalty parameter.

Problem.(6) can be solved via the following alternating minimization method

$$\begin{cases} \mathbf{L}_{k+1} \in \arg \min_{\mathbf{L}} J(\mathbf{X}_k, \mathbf{L}, \mathbf{S}_k) \\ \mathbf{S}_{k+1} \in \arg \min_{\mathbf{S}} J(\mathbf{X}_k, \mathbf{L}_{k+1}, \mathbf{S}) \\ \mathbf{X}_{k+1} = \arg \min_{\mathbf{X}} J(\mathbf{X}, \mathbf{L}_{k+1}, \mathbf{S}_{k+1}) \end{cases} \quad (7)$$

Since the calculation of $(\mathbf{A}^* \mathbf{A} + \rho \mathbf{I})^{-1}$ is very time consuming, we attempt to solve the \mathbf{X} -subproblem inexactly. Particularly, for the \mathbf{X} -subproblem at Eq.(7), we can approximate the cost function J via linearizing the data fidelity $F(\mathbf{X}) := \frac{1}{2} \|\mathbf{A}\mathbf{X} - \mathbf{y}\|_2^2$ at $\hat{\mathbf{X}}_{k+1} := \mathbf{L}_{k+1} + \mathbf{S}_{k+1}$, i.e.,

$$\mathbf{X}_{k+1} = \arg \min_{\mathbf{X}} \tilde{J}_{k+1}(\mathbf{X}, \mathbf{L}_{k+1}, \mathbf{S}_{k+1}) \quad (8)$$

where

$$\begin{aligned} \tilde{J}_{k+1}(\mathbf{X}, \mathbf{L}_{k+1}, \mathbf{S}_{k+1}) := & \langle \nabla F(\hat{\mathbf{X}}_{k+1}), \mathbf{X} - \hat{\mathbf{X}}_{k+1} \rangle \\ & + \frac{1}{2\eta} \|\mathbf{X} - \hat{\mathbf{X}}_{k+1}\|_2^2 + \lambda_L \|\mathbf{L}_{k+1}\|_* \\ & + \lambda_S \|\mathbf{D}\mathbf{S}_{k+1}\|_1 + \frac{\rho}{2} \|\mathbf{L}_{k+1} + \mathbf{S}_{k+1} - \mathbf{X}\|_2^2 \end{aligned} \quad (9)$$

Thus the subproblems in Eq.(7) can be reformed as

$$\begin{cases} \mathbf{L}_{k+1} = \arg \min_{\mathbf{L}} \frac{\rho}{2} \|\mathbf{L} + \mathbf{S}_k - \mathbf{X}_k\|_2^2 + \lambda_{\mathbf{L}} \|\mathbf{L}\|_* \\ \mathbf{S}_{k+1} = \arg \min_{\mathbf{S}} \frac{\rho}{2} \|\mathbf{L}_{k+1} + \mathbf{S} - \mathbf{X}_k\|_2^2 + \lambda_{\mathbf{S}} \|\mathbf{D}\mathbf{S}\|_1 \\ \mathbf{X}_{k+1} = \arg \min_{\mathbf{X}} \frac{\rho}{2} \|\mathbf{L}_{k+1} + \mathbf{S}_{k+1} - \mathbf{X}\|_2^2 + \langle \nabla F(\hat{\mathbf{X}}_{k+1}), \mathbf{X} \rangle \\ \quad + \frac{1}{2\eta} \|\mathbf{X} - \hat{\mathbf{X}}_{k+1}\|_2^2 \end{cases} \quad (10)$$

Each of the three subproblems can be considered as a particular instance of the proximal gradient method. Given the assumption that $\hat{\mathbf{X}}_{k+1} = \mathbf{L}_{k+1} + \mathbf{S}_{k+1}$, the subproblems can be solved by iterating between the following update steps:

$$\begin{cases} \mathbf{L}_{k+1} = \mathbf{H}_{\lambda_{\mathbf{L}}}(\mathbf{X}_k - \mathbf{S}_k) \\ \mathbf{S}_{k+1} = \mathbf{P}_{\lambda_{\mathbf{S}}}(\mathbf{X}_k, \mathbf{L}_{k+1}) \\ \hat{\mathbf{X}}_{k+1} = \mathbf{L}_{k+1} + \mathbf{S}_{k+1} \\ \mathbf{X}_{k+1} = \hat{\mathbf{X}}_{k+1} - \gamma \nabla F(\hat{\mathbf{X}}_{k+1}) \end{cases} \quad (11)$$

where

$$\mathbf{H}_{\lambda}(\mathbf{X}) = \mathbf{U} \mathbf{\Lambda}_{\lambda}(\mathbf{\Sigma}) \mathbf{V}^* \quad (12)$$

is a singular value thresholding (SVT) operator. In Eq.(12), $\mathbf{X} = \mathbf{U} \mathbf{\Sigma} \mathbf{V}^*$ is the singular value decomposition of \mathbf{X} . $\mathbf{\Lambda}_{\lambda}$ is the soft thresholding operator as follow:

$$\mathbf{\Lambda}_{\lambda} = \frac{x}{|x|} \max(|x| - \lambda, 0). \quad (13)$$

In the rest three update steps in Eq.(11), $\mathbf{P}(\cdot)$ is a proximal operator depending on the sparse transform \mathbf{D} ; γ is a update step size that $\gamma = 1/(1 + \eta\rho)$. $\mathbf{H}_{\lambda_{\mathbf{L}}}$ forces the matrix to be low-rank by eliminate small singular values with the threshold of $\lambda_{\mathbf{L}}$. Because the last singular value are relatively small, some of them are suppressed to zero, lowering the rank of \mathbf{L} as a circumstance. The rank of \mathbf{L} is reduced at each iteration step, and finally \mathbf{L} becomes a slowly changing the background component. In the update step of \mathbf{X}_k , the gradient term is

$$\nabla F(\mathbf{X}) = \mathbf{A}^*(\mathbf{A}(\mathbf{X}) - \mathbf{y}), \quad (14)$$

so the \mathbf{X} update step is a kind of data consistence operation, where $\nabla F(\hat{\mathbf{X}}_{k+1})$ is the image-correction term of residual in k-space. specifically, for single coil imaging,

$$\nabla F(\mathbf{X}) = \mathbf{F}_u^*(\mathbf{F}_u(\mathbf{X}) - \mathbf{y}), \quad (15)$$

where \mathbf{F}_u is Fourier transform with undersampling, and \mathbf{F}_u^* is inverse Fourier transform; For multi-coil imaging,

$$\nabla F(\mathbf{X}) = \mathbf{S}^* \mathbf{F}_u^*(\mathbf{F}_u \mathbf{S}(\mathbf{X}) - \mathbf{y}), \quad (16)$$

which adds the coil sensitivities \mathbf{S} into the calculation. In traditional CS-MRI, the optimized \mathbf{L}^* and \mathbf{S}^* and \mathbf{X}^* can be obtain by iteratively solving Eq.(11).

Although the iterative steps are given, there are three intractable problems. First, because the proximal operator $\mathbf{P}(\cdot)$ is achieved via proximal gradient method, the closed form of it can only be achieved under the circumstance that the transform matrix \mathbf{D} is orthogonal (for example, temporal FFT). If a fixed orthogonal transform is adopted, the sparse representation will be limited. Otherwise, the calculation of $\mathbf{P}(\cdot)$ is not able to be performed due to the lack of its closed form. Second, the selection of the parameters $\lambda_{\mathbf{L}}$, $\lambda_{\mathbf{S}}$, γ is empirical. There is no guidance for parameter selection, thus the optimal parameters can only be found through repeated trails. This problem is particularly serious when the reconstruction time is long. Third, the algorithms in the iteration scheme usually takes a lot of steps before converge, which makes the reconstruction time very long.

The unrolling low-rank plus sparse network, dubbed as L+S-Net, tackles all the problems well. In the study, the iteration steps are unrolled into several iteration blocks. Each of the blocks contains three network modules as shown in Fig.1, which are named as low-rank prior layer \mathbf{L}^k , sparse prior layer \mathbf{S}^k , and data consistence layer \mathbf{X}^k corresponding to the \mathbf{L} , \mathbf{S} , \mathbf{X} update steps in Eq.(11):

$$\begin{cases} \mathbf{L}^{k+1} : & \mathbf{L}_{k+1} = \mathbf{H}_{\beta}(\mathbf{X}_k - \mathbf{S}_k) \\ \mathbf{S}^{k+1} : & \mathbf{S}_{k+1} = \mathbf{C}(\mathbf{X}_k, \mathbf{L}_{k+1}) \\ \mathbf{X}^{k+1} : & \mathbf{X}_{k+1} = \mathbf{L}_{k+1} + \mathbf{S}_{k+1} - \gamma \nabla F(\mathbf{L}_{k+1} + \mathbf{S}_{k+1}) \end{cases} \quad (17)$$

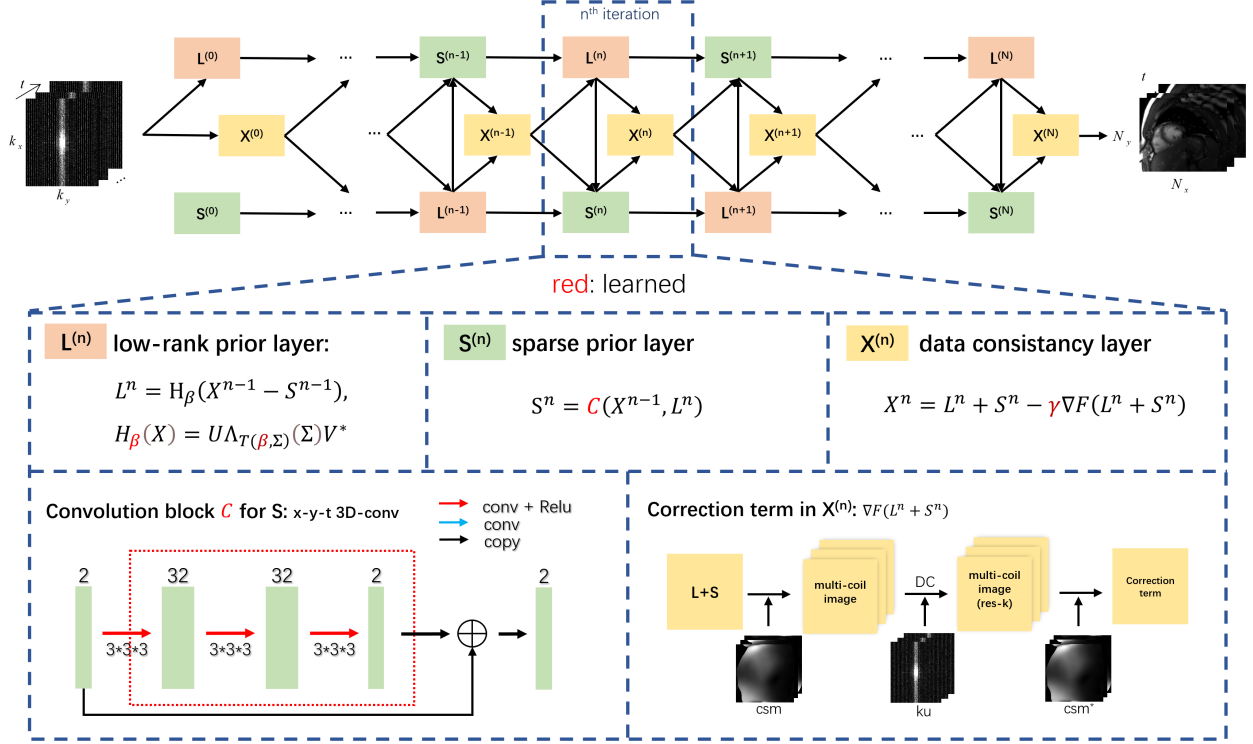


Figure 1: The proposed sparse plus low-rank network (L+S-Net) for dynamic MRI. The L+S-Net is defined over the iterative procedures of Eq.(17). The three layers in Eq.(17) correspond to the three modules in L+S-Net, which are named as low-rank prior layer L^n , sparse prior layer S^n and data consistence layer X^n respectively. The convolution block C in sparse prior layer S^n is shown in the left bottom. The correction term $\nabla F(L^n + S^n)$ in data consistence layer X^n is shown in the right bottom.

A) The low-rank layer L^k performs the learned soft threshold (LSVT) to $X_k - S_k$ according the L step in Eq.(11). The LSVT share the same calculation process with the traditional SVT as stated in Eq.(12), but the threshold λ_L of singular value thresholding operator H_{λ_L} is replaced with a learnable $T(\beta, \Sigma)$

$$H_{\beta}(X) = U \Lambda_{T(\beta, \Sigma)}(\Sigma) V^* \quad (18)$$

in which the threshold for soft threshold operator Λ is

$$T(\beta, \Sigma) = S(\beta) \cdot \sigma_1 \quad (19)$$

where σ_1 is the maximal singular value in singular value matrix Σ , and β is a learnable threshold factor. Sigmoid function S is employed to make sure the threshold $T(\beta, \Sigma)$ is less than the maximal singular value and larger than zero. After the LSVT, some of the small singular values are reduced to zero, which leads to the decreasing of the rank.

B) The sparse layer S^k in Eq.(17) use a residual 3D convolution neural network C to learn a customized proximal operator for each unrolling block, taking channel-stacked X_k and L_{k+1} as inputs. Therefore, the sparse transform is no more limited to orthogonal ones, instead, a more free transform D is implicitly learned through proximal operator during network training. At the meantime, the convolution process is calculable. Therefore, the first problem is solved.

C) The data consistence layer X^k has different form in single-coil imaging and multi-coil imaging as stated in Eq.(15) and Eq.(16). The multi-coil version is also illustrated in Fig.1.

The introduced learnable parameter β and proximal operator together automatically separate the L and S components in a optimal way.

To dealing with the second problem, the introduced parameters, including the threshold factor β , the update step γ and the CNN prixmal operator C , are learned during the network training, avoiding the empirical manual selection.

For the third problem, the unrolled network only contains several iteration blocks (usually less than 20), which corresponds to several steps in traditional iterative methods. The huge reduction in iteration steps (e.g. hundreds v.s. several) drives the total reconstruction time down as a circumstance.

All of these learnable parameters in the L+S-Net is different among each block, enables the network to get the optimal reconstruction in only several blocks. In the first unrolling block, the input L_0 is initialized to zero-filling image, and S_0 is initialized with zeros.

The formulated network should be trained before putting into use. Given a undersampled data as input and fully sampled image as ground truth, the network is trained by minimizing the pixel-wise mean-square error(MSE) between the reconstructed image Rec and the label image Ref . The loss is as follow:

$$\mathcal{L}(\theta) = \sum_M \sum_N \|Rec - Ref\|_2^2 \quad (20)$$

where θ is the network parameters to be optimized, N is the pixel number of a reconstruction image and M is the number of training data.

Because the number of iteration blocks corresponds to the iterative steps, the offline reconstruction will only take

3 Experimental results

3.1 Setup

3.1.1 Datasets

Two cardiac datasets were used in this work, one for retrospective study and the other for prospective study. The main experiments were conducted on the retrospective dataset to prove the effectiveness of the proposed method, and the prospective dataset was used to demonstrate the generalization performance.

1) Cardiac cine dataset for retrospective study:

The fully sampled cardiac cine data is collected from 29 healthy volunteers on a 3T scanner (MAGNETOM Trio, Siemens Healthcare, Erlangen, Germany) with a multi-channel receiver coil array (32 coils). All in vivo experiments were approved by the Institutional Review Board (IRB) of Shenzhen Institutes of Advanced Technology, and informed consent was obtained from each volunteer. For each subject, 10 to 13 short-axis slices were imaged with the retrospective electrocardiogram (ECG)-gated segmented bSSFP sequence during breath-hold. Total 386 slices were collected. The following sequence parameters were used: FOV = 330×330 mm, acquisition matrix = 256×256 , slice thickness = 6 mm, TR/TE = 3.0 ms/1.5 ms. The acquired temporal resolution was 40.0 ms and each data has about 25 phases that cover the entire cardiac cycle. Both single-coil and coil-compressed multi-coil data were prepared for the experiments. The raw multi-coil data of each frame was combined by the adaptive coil combine method [Walsh et al., 2000] to produce a single-channel complex-valued image. We randomly selected 25 volunteers for training and the rest for testing. Deep learning typically requires a large amount of data for training [35]. Therefore, we applied data augmentation using rigid transformation-shearing. We sheared the dynamic images along the x, y, and t directions. The sheared size was $192 \times 192 \times 18$ ($x \times y \times t$), and the stride along the three directions is 25, 25, and 7, respectively. Finally, we obtained 800 2D-t cardiac MR data of size $192 \times 192 \times 18$ ($x \times y \times t$) for training and 118 data for testing.

2) Cardiac cine dataset for prospective study:

The prospective cardiac cine dataset contains two parts: 57 slices of full sampled training data for finetuning and 7 prospectively undersampled data for test. Both the full sampled data and undersampled data are collected in the short-axis and long-axis view on 3T Siemens MAGNETOM Prisma machine using a bSSFP sequence with FOV= 800×300 mm, acquisition matrix= 384×144 , slice thickness = 8 mm, TR/TE = 38.4 ms/1.05 ms. The use number of receiver coil is 34 for all data. The readout dimension includes a factor of two oversampling, leading to the first dimension of FOV that is twice the value selected on the scanner. Both of the fully sampled data and the undersampled data are collected using bSSFP sequence. The undersampled data is collected in real-time mode under free-breathing conditions. Because the difference in scan scheme, the fully sampled data has an average frame number of 18, and the undersampled data has 65 frames for each. All of these data are part of the OCMR dataset, details can be found in [Chen et al., 2020].

3.1.2 Under sampling pattern

For fully sampled data in both of the two dataset, retrospective undersampling was performed to generate input/output pairs for network training or test. For each frame, we fully sampled frequency-encodes (along k_x) and undersampled phase-encodes (along k_y). Both random cartesian mask [Jung et al., 2007] and variable density incoherent spatiotemporal acquisition (VISTA) mask [Ahmad et al., 2015] were used in this work to demonstrate the generalization to different masks for our method. For single-coil experiments, we applied a randomly cartesian mask according to a zero-mean Gaussian variable density function, wherein 4 central phase-encodes were ensured to be sampled. For multi-coil data,

VISTA mask was used. The VISTA mask is based on a constrained minimization of Riesz energy on a spatiotemporal grid. VISTA mask is widely used in cs-based dynamic parallel imaging, therefore we choose it as the mask pattern for multi-coil reconstruction. The sampling mask for prospectively undersampled data is a 9-fold VISTA mask, which is defined in the MR scanner. Both of these two kinds of masks works well with out proposed model.

3.1.3 Coil sensitivity estimation for multi-coil data

For multi-coil data, the coil sensitivity maps were calculated from the undersampled time-averaged k-space using ESPIRiT algorithm. Because the time-averaged k-space cannot be fully filled at high acceleration factor (up to 16x), only the center(48×48) of the k-space is used for sensitivity estimation.

3.1.4 Model configuration

The main structure of the network is as shown in Fig.1. In the experiments, the L+S-Net is implemented with 10 iterative blocks, each of them has independent learnable parameters and convolution layers. In the sparse prior blocks, each of the convolution blocks in C is a residual CNN with 3 convolution layers. Because the convolution is designed for float point data, which is incapable of the complex data, we divided each input of C into two channels, where the channels stored real and imaginary parts. The first two layers of the convolution block has 32 convolution kernels, and the last one has 2 kernels to output the real and imaginary part of the residual respectively. The kernel size is $3 \times 3 \times 3$. Leaky Rectifier Linear Units (LeakyReLU) [Maas et al., 2013] were selected as the nonlinear activation functions after each convolution layer. The L_0 and X_0 is initialized with the zero filling image, and the S_0 is initialized with zeros. The initial values for the learned threshold factor β in Eq.(19) and the learned step size γ in Eq.(17) are -2 and 1, respectively.

During the training, the batch size was 1 due to the limited GPU memory. The exponential decay learning rate [Zeiler, 2012] was used in the training procedure, and the initial learning rate was set to 0.001 with a decay of 0.95. The training procedure stopped after 50 epochs, when the loss did not decreased any more.

For the prospective reconstruction, we finetuned the 8-fold pretrained L+S-Net on the fully sampled data in OCMR dataset, then the real-time undersampled data was tested on the finetuned model. The finetuning took 50 epochs as well.

The models were implemented in the open framework Tensorflow 2.2 [40] with CUDA and CUDNN support. The training and testing is on a GPU server with Ubuntu 16.04 LTS (64-bit) operating system. The server is equipped with an Intel Xeon Gold 5120 Processor Central Processing Unit (CPU) and Nvidia RTX 2080Ti Graphics Processing Unit (GPU, 11GB memory). in the open framework Tensorflow 2.2 [40] with CUDA and CUDNN support. The models were trained by the Adam optimizer [Kingma and Ba, 2014] with parameters $\beta_1 = 0.9$, $\beta_2 = 0.999$, and $\epsilon = 10^{-8}$. It took approximately 20 hours for 50 epochs to train the network from scratch, and about 2 hours for finetuning.

3.1.5 Performance evaluation

Both the visual comparison and quantitative evaluation is used for performance evaluation. For a quantitative evaluation, mean square error (MSE), peak signal to noise ratio (PSNR) and structural similarity index (SSIM) [Wang et al., 2004] were measured as follows:

$$\text{MSE} = \|Ref - Rec\|_2^2 \quad (21)$$

$$\text{PSNR} = 20 \log_{10} \frac{\max(Ref)\sqrt{N}}{\|Ref - Rec\|_2} \quad (22)$$

$$\text{SSIM} = \mathbf{l}(Ref, Rec) \cdot \mathbf{c}(Ref, Rec) \cdot \mathbf{s}(Ref, Rec) \quad (23)$$

where Rec is the reconstructed image, Ref denotes the reference image and N is the total number of image pixels. The SSIM index is a multiplicative combination of the luminance term, the contrast term, and the structural term (details shown in [Wang et al., 2004]). Higher PSNR and SSIM and lower MSE means better quantitative performance.

3.2 The reconstruction performance of the proposed L+S-Net

3.2.1 The seperation of L and S components

The seperation of L and S components meets the hypothesis of low-rank plus sparse. The reconstruction result $L + S$, together with its static component L and dynamic component S is shown in Fig.2(a). To demonstrate the low-rank and sparse features, y-t view of the decomposition is shown in Fig.2(b). From the y-t view, we can clearly observe that the

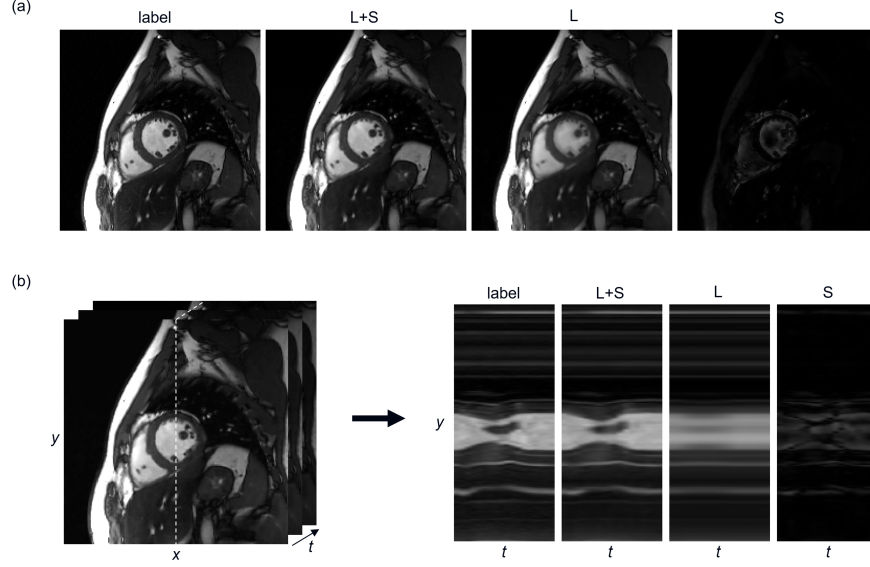


Figure 2: The L and S components separation results of the proposed L+S-Net at 8-fold acceleration. (a) the x-y view of the label image, the reconstruction result, the reconstructed L component and S component. (b) The left part is a demonstration of the reconstructed results by L+S-Net, the right part corresponds to the y-t view at the white center line in the reconstruction image. The L component is slowly changing over time and contains the most correlated component of the cardiac motion, rather than static. The S component is sparse even without a sparse transform.

Table 1: The average MSE, PSNR, SSIM of L+S-Net at 8-fold, 10-fold and 12-fold acceleration on the cardiac cine test dataset (mean \pm std).

AF	Methods	MSE(*e-5)	PSNR (dB)	SSIM(*e-2)
8x	L+S	11.54 \pm 5.12	39.75 \pm 1.75	94.46 \pm 1.68
	DCCNN	7.43 \pm 2.33	41.48 \pm 1.30	96.22 \pm 0.76
	CRNN	5.60 \pm 1.67	42.7 \pm 1.24	97.07 \pm 0.61
	S-Net	4.97 \pm 1.76	43.28 \pm 1.47	97.21 \pm 0.76
	L+S-Net	2.91\pm1.25	45.72\pm1.72	98.23\pm0.61
10x	CRNN	7.28 \pm 2.25	41.58 \pm 1.31	96.49 \pm 0.75
	DCCNN	11.07 \pm 3.13	39.73 \pm 1.21	94.61 \pm 0.87
	L+S-Net	4.39\pm1.60	43.83\pm1.50	97.68\pm0.68
12x	CRNN	11.87 \pm 3.35	39.43 \pm 1.21	94.57 \pm 0.89
	DCCNN	12.98 \pm 3.62	39.03 \pm 1.19	93.78 \pm 0.87
	L+S-Net	4.94\pm1.89	43.35\pm1.57	97.40\pm0.77

L component is a slowly changing background rather than a static one. The low-rank property holds well in the test dataset. As can be seen from Fig.2 the S component is already sparse without sparse transform, which means the it may has a sparser representation after the transform corresponding to the learned proximal operator P .

3.2.2 Comparison study for single-coil data

The comparison between the unrolled L+S-Net and iterative L+S method at 8-fold acceleration is shown in Fig.3. The first row shows the ground truth and the reconstruction results for these two methods. The second row shows the magnified view of the heart region framed with the yellow boxes. The third row shows the error map of the ROI region. The y-t images at x=92, is shown in the forth row, and the error maps of y-t images are also given in the last row. The display ranges for all of the gray images and error maps are $[0, 0.3]$ and $[0, 0.07]$, respectively. It is obvious that the L+S-Net has an advantage over the traditional L+S method at 8-fold acceleration. The image reconstructed using L+S-Net appears to be much cleaner than the L+S method, while the L+S method exhibits artifacts within the chambers. The error of L+S is much larger than the proposed method, especially around the edge of papillary muscle. From the y-t view, the proposed L+S-Net captures the dynamic information more precisely.

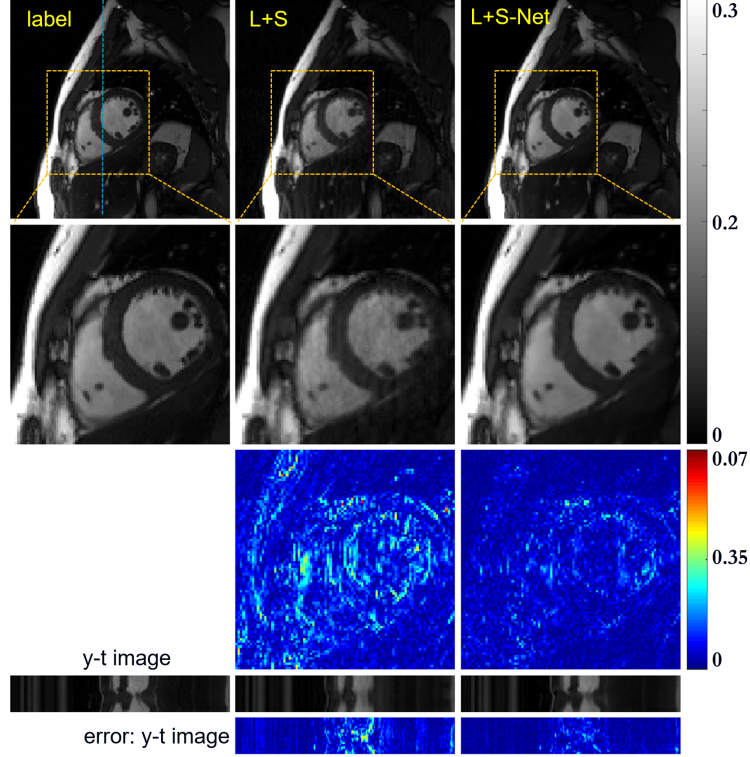


Figure 3: The reconstruction results of the L+S and L+S-Net at 8-fold acceleration. The first row shows, from left to right, the ground truth, the reconstruction result of these methods. The second row shows the enlarged view of their respective heart regions framed by a yellow box. The third row shows the error map (display ranges $[0, 0.07]$). The y-t image (extraction of the 92th slice along the y and temporal dimensions) and the error of y-t image are also given for each signal to show the reconstruction performance in the temporal dimension.

Our proposed method exhibits better performance than the state-of-the-art reconstruction methods as well. Fig.4 depicts the reconstruction results at 8-fold acceleration for cardiac cine dataset. The proposed method outperforms CRNN and DCCNN, which can be clearly seen from the error maps. The comparison between these methods shows that L+S-Net performs better than other methods in both detail retention and artifact removal (as shown by the green and red arrows). The comparison between the L+S-Net and S-Net (same network structure as L+S-Net without the low-rank prior layers) shows that, with low-rank prior, the L+S-Net exhibits better performance in detail reconstruction and contrast, which leads to the lower error level around edges and high-frequency areas. The result indicates that the low-rank prior is critical for the improvement in dynamic MR reconstruction.

The quantitative evaluation is shown in Table.1. Corresponding to the visual comparison result, the L+S-Net achieve the best quantitative performance. Therefore, the proposed L+S-Net can effectively explore the low-rank prior in a learning way, and improve the reconstruction quality consequencely.

The proposed L+S-Net uses not only the sparse prior, but also the low-rank prior in the dynamic images. Using more regularization terms in the optimization problem improves the reconstruction performance a lot, making higher acceleration factor become possible. We tested our proposed L+S-Net with higher undersampling rate at 10-fold and 12-fold on the cardiac cine dataset, to show its potential in highly undersampled imaging. Fig.5 shows the 10-fold and 12-fold accelerated reconstruction results. The proposed L+S-Net shows superior performance all the way through. At 10-fold acceleration, the L+S-Net outputs images with good anatomical details of the heart and the papillary muscle near the boundary is still clear. At 12-fold acceleration, the reconstructed image is still acceptable. Most of the details such as the papillary muscle near the boundary is still noticeable, although high frequency details in the images, mostly around the edge of the cardiac muscle are slightly blurry. The quantitative metrics are given in Table.??, whcih shows that the proposed L+S-Net still have good performance at higher acceleration factor.

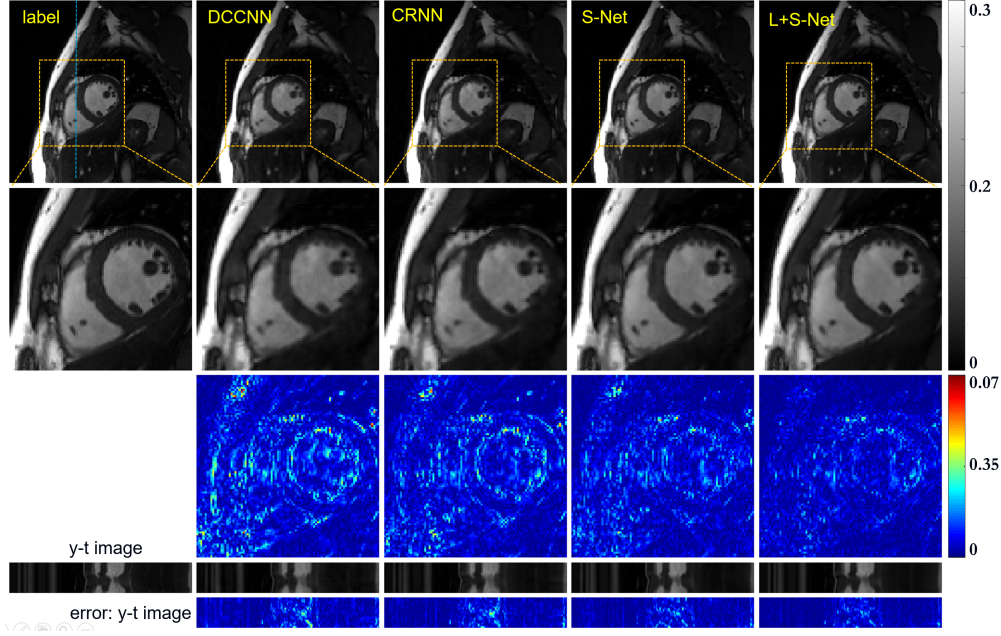


Figure 4: The reconstruction results of the different methods (DC-CNN, CRNN, S-Net and L+S-Net) at 8-fold acceleration. The first row shows, from left to right, the ground truth, the reconstruction result of these methods. The second row shows the enlarged view of their respective heart regions framed by a yellow box. The third row shows the error map (display ranges $[0, 0.07]$). The y-t image (extraction of the 92th slice along the y and temporal dimensions) and the error of y-t image are also given for each signal to show the reconstruction performance in the temporal dimension.

Table 2: The average reconstruction time for different methods both on single-coil data and multi-coil data.

	L+S	DCCNN	CRNN	S-Net	MoDL	L+S-Net
single (s)	40.12	0.43	0.69	0.66	-	1.15
multi (s)	94.56	-	-	-	0.80	1.30

3.2.3 Multi-coil reconstruction

Our proposed L+S-Net performs well on multi-coil dynamic MR data. Fig.6 shows the comparison between the results of L+S, MoDL and the proposed L+S-Net at the acceleration factor of 12. L+S almost failed at such a high acceleration rate, the reconstruction result of which shows a lot of artifacts. The deep-learning-based MoDL method achieve acceptable results. We can see the proposed L+S-Net performs better, especially from the error map, . To our best knowledge, our work is the first one to apply low-rank prior in unrolled deep learning MRI reconstruction.

3.2.4 Prospective study on real-time OCMR data

The free-breathing 9-fold undersampled cardiac dataset described in the section 3.1.1(2) was reconstructed using L+S, MoDL and L+S-Net. The MoDL and L+S-Net is finetuned on the full sampled OCMR dataset. The visual comparison is shown in Fig.7. Because the spatial resolution is relatively lower than data in the retrospective study, the image quality of the images in this part is not as good as the former ones. The two deep-learning-based methods are superior to the iterative L+S method, showing lower streaking artifacts and spatial blurring. From the x-y view, The results of MoDL method still have some artifacts, while the results of L+S-Net are cleaner. From the y-t view, the edges of the image that reconstructed using L+S-Net are sharper than the others, which means the L+S-Net is better at capturing the dynamic information. The quantitative comparisons is not given since the ground truth dataset was not available.

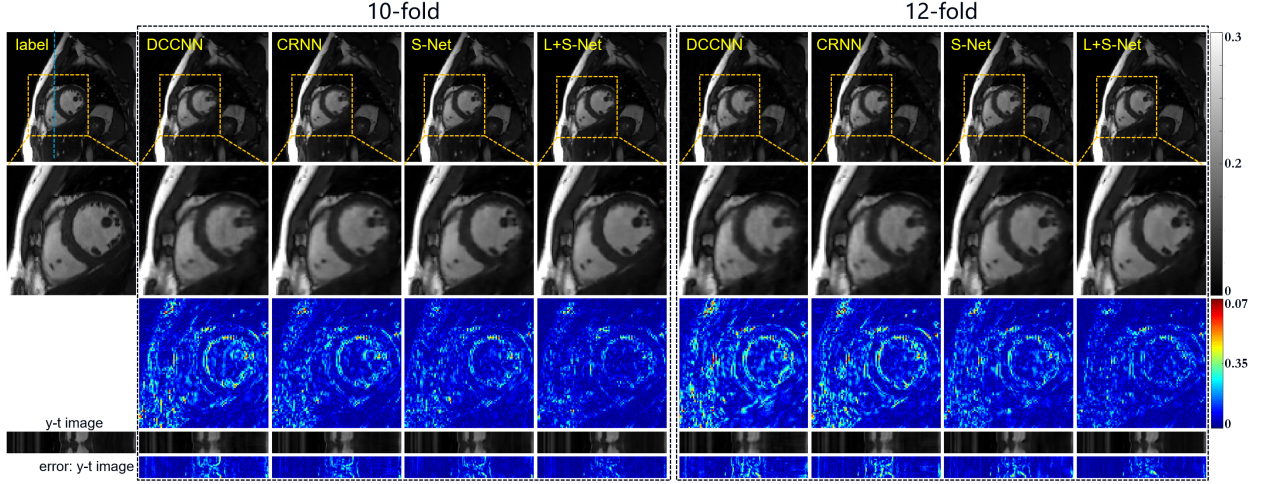


Figure 5: The reconstruction results of the proposed L+S-Net at 10-fold and 12-fold acceleration on cardiac cine dataset. The left half shows 10-fold reconstruction, and the right half shows 12-fold reconstruction. The first row shows, from left to right, the ground truth and the reconstruction result of these methods. The second row shows the enlarged view of their respective heart regions framed by a yellow box. The third row shows the error map (display ranges $[0, 0.07]$). The y-t image (extraction of the 92th slice along the y and temporal dimensions) and the error of y-t image are also given for each signal to show the reconstruction performance in the temporal dimension.

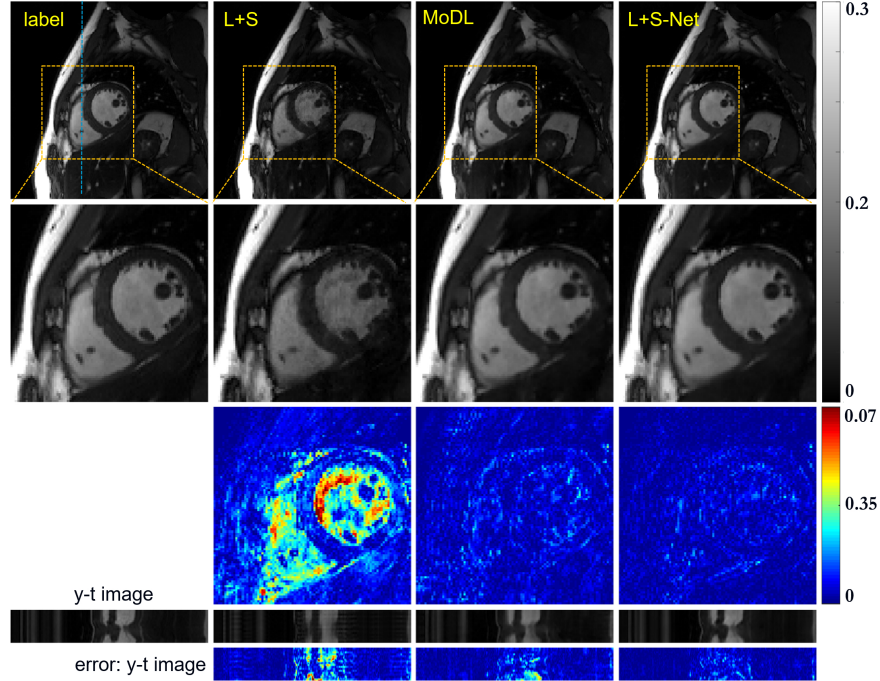


Figure 6: The reconstruction results of the different methods (L+S, MoDL and L+S-Net) at 12-fold acceleration using multi-coil data. The first row shows, from left to right, the ground truth, the reconstruction result of these methods. The second row shows the enlarged view of their respective heart regions framed by a yellow box. The third row shows the error map (display ranges $[0, 0.07]$). The y-t image (extraction of the 92th slice along the y and temporal dimensions) and the error of y-t image are also given for each signal to show the reconstruction performance in the temporal dimension.

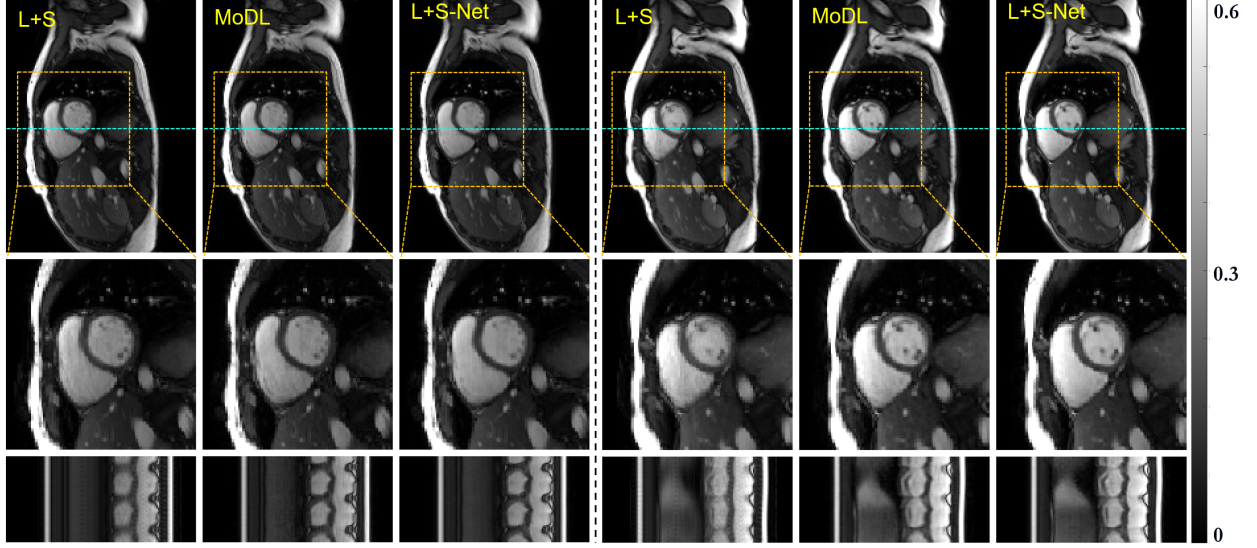


Figure 7: The prospective reconstruction results of L+S and the proposed L+S-Net at 9-fold acceleration. The left half and the right half shows 2 different test cases. The first row shows the full image at $t=18$. The second row shows the enlarged view of their respective heart regions framed by a yellow box. The third row shows the y-t images which extracted from the white lines in the images in the first row.

4 Discussion

4.1 The comparison of reconstruction time

The computation of SVD is very time-consuming, even when the reduced SVD is used. The iteration algorithms usually take dozens or hundreds of steps to converge, reduplicating the time of SVD. Therefore traditional low-rank methods in MRI reconstruction are very slow to reconstruct. In our method, we unrolled the iteration in to *ten* steps, which means only ten times of SVD are computed in a reconstruction procedure. It greatly reduced the computation time. The average time used for reconstructing a dynamic series is list in the last column in Table.2. The traditional iterative L+S methods takes much longer time than the other deep-learning-based methods, especially when reconstructing images from undersampled multi-coil data. The proposed L+S-Net consumes slightly longer time than other deep learning methods that compared in this work. Although the introduction of deep low-rank increases the amount of computation the SVD procedure in L+S-Net, the effect on the reconstruction time is very small comparing to the sparse-based deep learning methods, and can even be ignored when compared with the reconstruction time of traditional CS methods.

4.2 Very high acceleration reconstruction

Because the multi-coil reconstruction result of L+S-Net is still acceptable at 12-fold acceleration, we explored its performance at higher acceleration factor: 16-fold, 20-fold and 24-fold. The reconstruction results and error maps are shown in Fig.8. The details in both of the two results are acceptable. Our approach can still recover the dynamic content of the image very well on such extremely undersampled data, although the artifacts near the boundary is a little bit stronger at 24-fold. From the y-t view, the results of our proposed method are still acceptable for all the three acceleration factors, but at 24-fold, the dynamic information loss is a bit large comparison to 16-fold and 20-fold. The reconstruction result at extremely high acceleration rate indicates that the proposed method has great potential in high-resolution dynamic imaging.

4.3 The limitations of the proposed method

Although the proposed L+S-Net achieved good reconstruction results, it still has some limitations. First, the scheme to learn the low-rank prior in our proposed method does not avoid the calculation of SVD which caused heavy computation. SVT is one of the many methods that can explore the low-rank prior. Further works need to be done to explore if there is a better low-rank prior scheme can be use in L+S-Net, such as methods with Hankel matrix, which can avoid the calculation of SVD. Second, The L+S-Net is not suitable for the tasks in which the image has no low-rank plus sparse

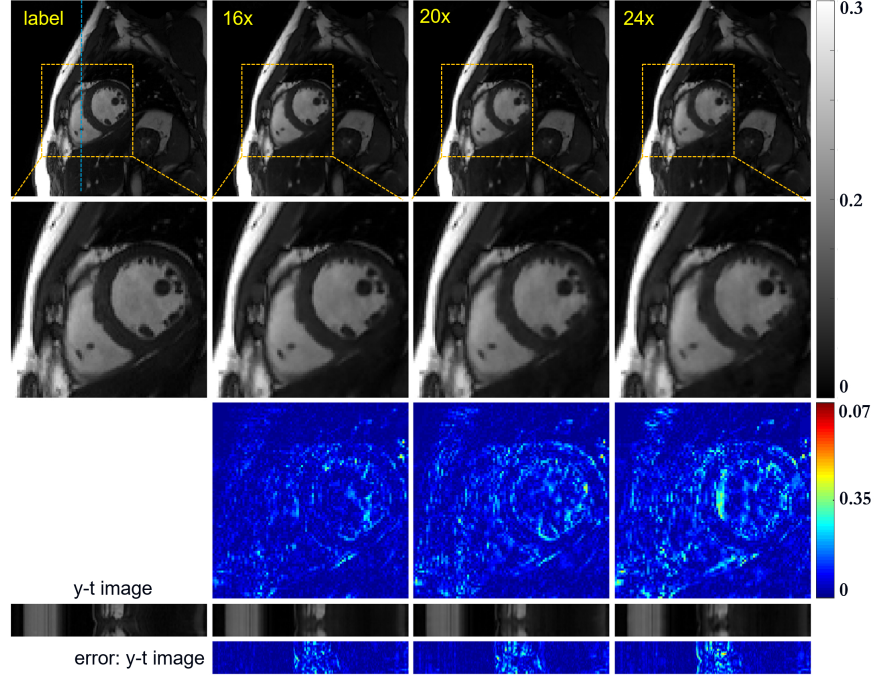


Figure 8: The reconstruction results of the proposed L+S-Net at 16-fold, 20-fold and 24-fold accelerations on cardiac cine dataset. The first row shows, from left to right, the ground truth and the reconstruction result of these methods. The second row shows the enlarged view of their respective heart regions framed by a yellow box. The third row shows the error map (display ranges $[0, 0.07]$). The y-t image (extraction of the 92th slice along the y and temporal dimensions) and the error of y-t image are also given for each signal to show the reconstruction performance in the temporal dimension.

property. So the application of the proposed method is limited. Third, the performance of the L+S-Net is not tested on other body parts except heart. More tests should be done on different dynamic imaging scenarios.

5 Conclusion and outlook

In this paper, we propose a model-based unrolled low-rank plus sparse network, dubbed as L+S-Net, for dynamic MR reconstruction. In particular, we used an alternating linearized minimization method to solve the optimization problem with low-rank and sparse regularization. A learned singular value thresholding was introduced to make sure the clear separation of L component and S component. Then the iterative steps are unrolled into a network whose regularization parameters are learnable. The proposed method was tested on two cardiac cine datasets. Experiment results show that our method can improved the reconstruction result both qualitatively and quantitatively.

Acknowledgments

This work was supported in part by the National Natural Science Foundation of China (61771463, 81830056, U1805261, 81971611, 61871373, 81729003, 81901736); National Key R&D Program of China (2017YFC0108802 and 2017YFC0112903); Natural Science Foundation of Guangdong Province (2018A0303130132); Shenzhen Key Laboratory of Ultrasound Imaging and Therapy (ZDSYS20180206180631473); Shenzhen Peacock Plan Team Program (KQTD20180413181834876); Innovation and Technology Commission of the government of Hong Kong SAR (MRP/001/18X); Strategic Priority Research Program of Chinese Academy of Sciences (XDB25000000)

References

Ahmad, R., Xue, H., Giri, S., Ding, Y., Craft, J., Simonetti, O.P., 2015. Variable density incoherent spatiotemporal acquisition (vista) for highly accelerated cardiac mri. *Magnetic resonance in medicine* 74, 1266–1278.

- Ashikuzzaman, M., Belasso, C., Kibria, M.G., Bergdahl, A., Gauthier, C.J., Rivaz, H., 2019. Low rank and sparse decomposition of ultrasound color flow images for suppressing clutter in real-time. *IEEE transactions on medical imaging* 39, 1073–1084.
- Caballero, J., Price, A.N., Rueckert, D., Hajnal, J.V., 2014. Dictionary learning and time sparsity for dynamic mr data reconstruction. *IEEE transactions on medical imaging* 33, 979–994.
- Candès, E.J., Li, X., Ma, Y., Wright, J., 2011. Robust principal component analysis? *Journal of the ACM (JACM)* 58, 1–37.
- Chandrasekaran, V., Sanghavi, S., Parrilo, P.A., Willsky, A.S., 2011. Rank-sparsity incoherence for matrix decomposition. *SIAM Journal on Optimization* 21, 572–596.
- Chen, C., Liu, Y., Schniter, P., Tong, M., Zareba, K., Simonetti, O., Potter, L., Ahmad, R., 2020. Ocmr (v1. 0)–open-access dataset for multi-coil k-space data for cardiovascular magnetic resonance imaging. *arXiv preprint arXiv:2008.03410*.
- Cheng, J., Wang, H., Ying, L., Liang, D., 2019. Model learning: Primal dual networks for fast mr imaging, in: *International Conference on Medical Image Computing and Computer-Assisted Intervention*, Springer. pp. 21–29.
- Donoho, D.L., 2006. Compressed sensing. *IEEE Transactions on information theory* 52, 1289–1306.
- Gao, H., Cai, J.F., Shen, Z., Zhao, H., 2011. Robust principal component analysis-based four-dimensional computed tomography. *Physics in Medicine & Biology* 56, 3181.
- Han, Y., Yoo, J., Kim, H.H., Shin, H.J., Sung, K., Ye, J.C., 2018. Deep learning with domain adaptation for accelerated projection-reconstruction mr. *Magnetic resonance in medicine* 80, 1189–1205.
- Jung, H., Ye, J.C., Kim, E.Y., 2007. Improved k–t blast and k–t sense using focuss. *Physics in Medicine & Biology* 52, 3201.
- Kingma, D.P., Ba, J., 2014. Adam: A method for stochastic optimization. *arXiv preprint arXiv:1412.6980*.
- Kwon, K., Kim, D., Park, H., 2017. A parallel mr imaging method using multilayer perceptron. *Medical physics* 44, 6209–6224.
- Liang, D., Cheng, J., Ke, Z., Ying, L., 2020. Deep magnetic resonance image reconstruction: Inverse problems meet neural networks. *IEEE Signal Processing Magazine* 37, 141–151.
- Lingala, S.G., Hu, Y., DiBella, E., Jacob, M., 2011. Accelerated dynamic mri exploiting sparsity and low-rank structure: kt slr. *IEEE transactions on medical imaging* 30, 1042–1054.
- Lustig, M., Donoho, D., Pauly, J.M., 2007. Sparse mri: The application of compressed sensing for rapid mr imaging. *Magnetic Resonance in Medicine: An Official Journal of the International Society for Magnetic Resonance in Medicine* 58, 1182–1195.
- Lustig, M., Elad, M., Pauly, J., 2010. Calibrationless parallel imaging reconstruction by structured low-rank matrix completion, in: *Proceedings of the 18th Annual Meeting of ISMRM, Stockholm*, p. 2870.
- Ma, S., Yin, W., Zhang, Y., Chakraborty, A., 2008. An efficient algorithm for compressed mr imaging using total variation and wavelets, in: *2008 IEEE Conference on Computer Vision and Pattern Recognition*, IEEE. pp. 1–8.
- Maas, A.L., Hannun, A.Y., Ng, A.Y., 2013. Rectifier nonlinearities improve neural network acoustic models, in: *Proc. icml*, p. 3.
- Mansour, H., Vetro, A., 2014. Video background subtraction using semi-supervised robust matrix completion, in: *2014 IEEE International Conference on Acoustics, Speech and Signal Processing (ICASSP)*, IEEE. pp. 6528–6532.
- Nakarmi, U., Wang, Y., Lyu, J., Ying, L., 2015. Dynamic magnetic resonance imaging using compressed sensing with self-learned nonlinear dictionary (nl-d), in: *2015 IEEE 12th International Symposium on Biomedical Imaging (ISBI)*, IEEE. pp. 331–334.
- Otazo, R., Candes, E., Sodickson, D.K., 2015. Low-rank plus sparse matrix decomposition for accelerated dynamic mri with separation of background and dynamic components. *Magnetic resonance in medicine* 73, 1125–1136.
- Otazo, R., Kim, D., Axel, L., Sodickson, D.K., 2010. Combination of compressed sensing and parallel imaging for highly accelerated first-pass cardiac perfusion mri. *Magnetic resonance in medicine* 64, 767–776.
- Peng, Y., Ganesh, A., Wright, J., Xu, W., Ma, Y., 2012. Rasl: Robust alignment by sparse and low-rank decomposition for linearly correlated images. *IEEE transactions on pattern analysis and machine intelligence* 34, 2233–2246.
- Qin, C., Schlemper, J., Caballero, J., Price, A.N., Hajnal, J.V., Rueckert, D., 2018. Convolutional recurrent neural networks for dynamic mr image reconstruction. *IEEE transactions on medical imaging* 38, 280–290.

- Schlemper, J., Caballero, J., Hajnal, J.V., Price, A.N., Rueckert, D., 2017. A deep cascade of convolutional neural networks for dynamic mr image reconstruction. *IEEE transactions on Medical Imaging* 37, 491–503.
- Walsh, D.O., Gmitro, A.F., Marcellin, M.W., 2000. Adaptive reconstruction of phased array mr imagery. *Magnetic Resonance in Medicine: An Official Journal of the International Society for Magnetic Resonance in Medicine* 43, 682–690.
- Wang, S., Cheng, H., Ying, L., Xiao, T., Ke, Z., Zheng, H., Liang, D., 2020. Deepcomplexmri: Exploiting deep residual network for fast parallel mr imaging with complex convolution. *Magnetic Resonance Imaging* 68, 136–147.
- Wang, S., Ke, Z., Cheng, H., Jia, S., Ying, L., Zheng, H., Liang, D., 2019. Dimension: Dynamic mr imaging with both k-space and spatial prior knowledge obtained via multi-supervised network training. *NMR in Biomedicine* , e4131.
- Wang, S., Su, Z., Ying, L., Peng, X., Zhu, S., Liang, F., Feng, D., Liang, D., 2016. Accelerating magnetic resonance imaging via deep learning, in: 2016 IEEE 13th International Symposium on Biomedical Imaging (ISBI), IEEE. pp. 514–517.
- Wang, Y., Ying, L., 2013. Compressed sensing dynamic cardiac cine mri using learned spatiotemporal dictionary. *IEEE transactions on Biomedical Engineering* 61, 1109–1120.
- Wang, Z., Bovik, A.C., Sheikh, H.R., Simoncelli, E.P., 2004. Image quality assessment: from error visibility to structural similarity. *IEEE transactions on image processing* 13, 600–612.
- Zeiler, M.D., 2012. Adadelta: an adaptive learning rate method. *arXiv preprint arXiv:1212.5701* .
- Zhao, B., Haldar, J.P., Christodoulou, A.G., Liang, Z.P., 2012. Image reconstruction from highly undersampled (k, t)-space data with joint partial separability and sparsity constraints. *IEEE transactions on medical imaging* 31, 1809–1820.